Journal of Electrochemistry

Volume 30
Issue 10 *Special Issue on Single-Entity Electroanalysis*

2024-10-28

Highly Sensitive Detection of Strontium Ions Using Metal-Organic Frameworks Functionalized Solid-State Nanochannels

Xu-Gang Wang

Zheng-Xu He

De-Fang Ding

Xue-Qin Luo

Li Dai

Wei-Qi Zhang

Qun Ma

See next page for additional authors

Highly Sensitive Detection of Strontium Ions Using Metal-Organic Frameworks Functionalized Solid-State Nanochannels

Authors

Xu-Gang Wang, Zheng-Xu He, De-Fang Ding, Xue-Qin Luo, Li Dai, Wei-Qi Zhang, Qun Ma, Yu Huang, and Fan Xia

Corresponding Author(s)

Yu Huang(yuhuang@cug.edu.cn)

ARTICLE

Single-Entity Electroanalysis

Highly Sensitive Detection of Strontium Ions Using Metal-Organic Frameworks Functionalized Solid-state Nanochannels

Xu-Gang Wang [a], Zheng-Xu He [a], De-Fang Ding [a], Xue-Qin Luo [a], Li Dai [a], Wei-Qi Zhang [a], Qun Ma [b], Yu Huang [a,*], Fan Xia [a,c]

[a] State Key Laboratory of Biogeology and Environmental Geology, Engineering Research Center of Nano-Geomaterials of Ministry of Education, Faculty of Material Science and Chemistry, China University of Geosciences, Wuhan 430074, PR China
[b] Department of Chemical Engineering, Graduate School of Engineering, Osaka Metropolitan University, Sakai, Osaka, 599-8570, Japan
[c] Shenzhen Research Institute of China University of Geosciences, Shenzhen 518052, Guangdong, PR China

Abstract

Strontium-90, a highly radioactive isotope, accumulates within the food chain and skeletal structure, posing significant risks to human health. There is a critical need for a sensitive detection strategy for Strontium-90 in complex environmental samples. Here, solid-state nanochannels, modified with metal-organic frameworks (MOF) and specific aptamers, were engineered for highly sensitive detection of strontium ion (Sr^{2+}). The synergistic effect between the reduced effective diameter of the nanochannels due to MOF and the specific binding of Sr^{2+} by aptamers amplifies the difference in ionic current signals, enhancing detection sensitivity significantly. The MOF-modified nanochannels exhibit highly sensitive detection of Sr^{2+}, with a limit of detection (LOD) being 0.03 nmol·L^{-1}, whereas the LOD for anodized aluminum oxide (AAO) without the modified MOF nanosheets is only 1000 nmol·L^{-1}. These findings indicate that the LOD of Sr^{2+} detected by the MOF-modified nanochannels is approximately 33,000 times higher than that by the nanochannels without MOF modification. Additionally, the highly reliable detection of Sr^{2+} in various water samples was achieved, with a recovery rate ranging from 94.00% to 118.70%. This study provides valuable insights into the rapidly advancing field of advanced nanochannel-based sensors and their diverse applications for analyzing complex samples, including environmental contaminant detection, food analysis, medical diagnostics, and more.

Keywords: Nanochannel; Metal-organic frameworks; Sensor; Strontium ion; Sensitivity detection

1. Introduction

The ocean stands as Earth's most vital natural resources crucial for human survival. Ocean monitoring serves as a crucial method for real-time observation and data collection in marine environments, playing a fundamental role in safeguarding marine ecosystems, and ensuring human sustenance and progress [1,2]. Especially, due to the recent Fukushima nuclear wastewater discharge incident in Japan, marine life is facing numerous uncertainties. Hence, the monitoring of the marine environment, particularly the surveillance of radioactive elements in seawater, has garnered escalating significance in scientific researches [3,4].

Traditionally, offshore marine water quality monitoring relies on manual sampling, involving the collection of samples by vessels at specific locations, followed by analysis and processing in onshore laboratories [5]. Current water quality monitoring technologies in laboratories mainly rely

Received 30 April 2024; Received in revised form 18 May 2024; Accepted 11 June 2024
Available online 23 July 2024

* Corresponding author, Yu Huang, E-mail address: yuhuang@cug.edu.cn.

https://doi.org/10.61558/2993-074X.3482

on physicochemical monitoring methods such as atomic absorption spectrophotometry [6], ion-selective electrode method [7,8], ion chromatography [9], gas chromatography [10], and inductively coupled plasma atomic emission spectroscopy (ICP-AES) [11]. Utilizing traditional manual sampling and laboratory detection technologies enables the accurate acquisition of samples, flexibility in selecting sampling locations, and a thorough assessment of water quality. However, this method is susceptible to weather and sea conditions, and exhibits low efficiency, particularly when monitoring radioactive elements like Strontium-90. The challenge lies in the large amount of sample requirements to detect trace amount of these elements in seawater, necessitating complex enrichment processes before analysis. Furthermore, current analytical methods entail intricate instrument operation, cumbersome sample handling procedure, slow response time, and limited timeliness. Consequently, there is an urgent call for the development of a portable sensor capable of rapid enrichment, simplified processing, and high sensitivity of radioactive elements in the ocean.

In recent decades, solid-state nanochannels have emerged as chemically and mechanically stable platforms [12–14], offering adjustable dimensions and exceptional enrichment capacity. These attributes address the limitations of traditional methods for trace element enrichment. Moreover, the confined space within nanochannels, coupled with their functionalization strategies, presents a distinct advantage for detection [15–17]. The integration of aptamers into nanochannel sensors through chemical modifications on the nanochannel surface has demonstrated remarkable sensitivity and specificity in target detection [18–22]. Notably, commercial anodized aluminum oxide (AAO) featuring an arrayed nanochannel structure within the 30–200 nm range is extensively employed in constructing solid-state nanochannel-based sensing platforms [23]. For example, Kuang's research group first modified the penicillamine molecule on copper selenide nanoparticles, and then self-assembled the nanoparticles onto AAO to form heterogeneous nanochannels to construct a sensing system. The detection of limit (LOD) as low as 0.027 nmol·L^{-1} was achieved [24]. Zeng et al. devised a sensing system employing AAO and mesoporous silica for dopamine detection, achieving a LOD of 0.1 nmol·L^{-1} [25]. Our research group used AAO to achieve ultra-high sensitivity and specificity for the detection of proteins [26]. On the other hand, leveraging the advantages of Metal-Organic Frameworks (MOF), such as high porosity, large specific surface area, and adjustable structure, MOF-modified nanochannels are regarded as advanced chemical sensors [27–31]. Therefore, with the organic ligand TCPP utilizing aluminum ions provided by AAO to synthesize two-dimensional nanosheets Al-TCPP (MOF) in-situ, modifying the inner and outer surfaces of AAO nanochannels, we chose this material to investigate the sensing performance toward strontium ion (Sr^{2+}). However, the direct use of MOF-modified nanochannels for detecting radioactive elements in complex water samples has not yet widespread, and their specific sensing properties in this context remain to be fully elucidated.

Here, a highly sensitive method for detecting Sr^{2+} in complex water samples was developed by synthesizing binary MOF nanosheets directly on AAO substrate (Scheme 1). This method involves modifying a DNA strand capable of folding into G-quadruplexes in response to Sr^{2+}, serving as specific probes (referred to as APT) on the surface of MOF-modified AAO (APT/MOF/AAO). During the recognition process of Sr^{2+}, the effective pore size of the nanochannels was significantly reduced due to the synergistic effect of specific aptamers

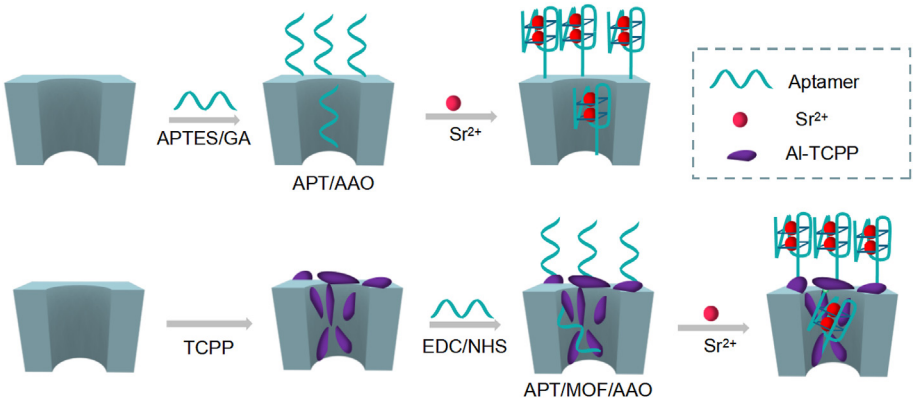

Scheme 1. Schematic diagram of the principle for the aptasensor. It describes the construction of two sensing systems, APT/AAO and APT/MOF/AAO, as well as the process of target identification.

and uniformly dispersed two-dimensional (2D) nanosheets on both the inner and outer surfaces of the AAO. This resulted in a considerable amplification of the variance in the ionic current signal, showcasing ultra-high sensitivity. Consequently, compared to the APT/AAO detection system, the APT/MOF/AAO detection system significantly improved the LOD from 1000 nmol·L^{-1} to an ultra-low 0.03 nmol·L^{-1}, which is lower than the Sr^{2+} concentration in natural seawater (90.1 μmol·L^{-1}), and the Sr^{2+} concentration in nuclear wastewater (0.1 μmol·L^{-1} to 1 mmol·L^{-1}) [32]. Additionally, the general ionic conductivity model of cylindrical nanochannels was employed to elucidate the sensing mechanism of the nanochannels. COMSOL was also utilized to simulate the increase in ion currents before and after the binding of nanochannels to the target, yielding the calculated results that align with the experimental findings. Furthermore, APT/MOF/AAO demonstrated the ability to accurately detect Sr^{2+} at nanomolar levels in complex samples such as tap water and mineral water. This research offers valuable insights into the burgeoning domain of advanced nanochannel-based sensors and their diverse applications for complex samples, spanning environmental contaminant detection, food analysis, medical diagnostics, and beyond.

2. Experimental Section

2.1. Chemicals and materials

The AAO membranes, with the height of 60 μm and the pore size of 80~100 nm, were purchased from Pu Yuan Nano (Hefei, China). Tetras-(4-carboxyphenyl) porphyrin (TCPP), N,N-dimethylformamide (DMF, 99%), isopropanol, and glutaraldehyde 25% aqueous solution were purchased from Sinopharm (Beijing, China). 1-Ethyl-3-(3-dimethylaminopropyl) carbodiimide (EDC), N-hydroxysulfosuccinimide sodium salt (NHS), 3-aminopropyltriethoxysilane (APTES), strontium chloride, Tris-HCl buffer, and PBS buffer were purchased from Aladdin (Shanghai, China). Single-stranded Aptamers (5′-NH_2-C6-AGGGTTAGGGTTAGGGTTAGGGC-3′) for Sr^{2+} sensing was purchased from Sangon Biotech Inc. (Shanghai, China). All solutions were made with deionized water (18.2 MΩ·cm, Milli-Q system).

2.2. Preparation of APT/AAO

Firstly, the AAO was placed in ultrapure water to sonicate for 5 min to remove surface impurities and dried at 60 °C for 5 min. Then, the dried AAO was immersed in a pre-prepared 15% APTES isopropanol solution to seal the shading reaction for 12 h. After the reaction was completed, it was washed three times with isopropanol to remove any unreacted APTES. Subsequently, the sample was dried in a 120 °C oven for 2 h to obtain the APTES-modified AAO. Afterwards, 5% glutaraldehyde aqueous solution was added, which was also sealed for 12 h, and then repeatedly rinsed with deionized water three times to remove the unreacted glutaraldehyde to obtain the aldehyde-modified AAO. Finally, the aldehyde-modified AAO was placed in Tris-HCl buffer containing 1 μmol·L^{-1} Sr^{2+} specific aptamer for 12 h to obtain the aptamer-modified AAO, called APT/AAO.

2.3. Preparation of MOF

To fabricate nanochannel films with smaller and denser pore sizes, certain adjustments were implemented in the experiments, drawing from insights provided in previous literature. The specific experimental procedure was as follows: TCPP (40 mg) was added to a PTFE liner filled with 25 mL of DMF and ultrapure water mixture (V_{DMF}:V_{water} = 3:1), mixed evenly, and then sonicated at room temperature for 15 min. Then, the bare AAO membrane after sonication was placed on a PTFE scaffold and immersed in the mixture. The inner tank was put into the reaction kettle, and sealed and placed in an oven at 120 °C for 2 h to obtain the MOF modified AAO, which is named MOF. After the reaction was completed, the obtained MOF membranes were washed with DMF and deionized water, respectively, and dried at room temperature in an oven.

2.4. Preparation of ATP/MOF/AAO

To obtain an aptamer-modified MOF membrane (APT/MOF/AAO), the MOF membrane was immersed in PBS buffer (pH = 7.4) containing 1-ethyl-3-(3-dimethylaminopropyl) carbodiimide (50 mg·mL^{-1}) and N-hydroxysulfosuccinimide (25 mg·mL^{-1}) for 1 hour to activate the carboxyl groups on the film's surface. Subsequently, the membrane was rinsed three times with deionized water before being immersed in Tris buffer containing the aptamer (10 mmol·L^{-1} Tris, pH = 7.4) for 12 h [33] to obtain the APT/MOF/AAO. Any unbound aptamers were then removed using deionized water.

2.5. Characterizations of materials

The surface and cross-sectional morphologies of AAO and MOF were characterized by using scanning transmission electroscope (FESEM, SU8010, Hetachi). X-ray photoelectron spectroscopy (XPS) was used to characterize AAO, MOF, and APT/

MOF/AAO. The morphological characteristics of MOF grown on AAO was studied by using atomic force microscopy (AFM).

2.6. Current-voltage (I-V) tests

According to previous reports, the transmembrane current of the sample was measured in a customized dual electrode system transmembrane current testing device, which includes a pair of separated electrolytic cells, a pair of self-made Ag/AgCl electrodes, electrolyte, and an external picoampere meter (Keithley 6487, Jishili Instruments, USA). The electrolyte used in this work was 10 mmol·L^{-1} Tris HCl (pH = 7.4). The nanochannels membrane to be tested was sandwiched between two electrolyzers and an electric field was applied as a scanning voltage ranging from −1 V to 1 V. Its current-voltage value was recorded by Keithley 6487 picoampere meter. All tests were conducted at room temperature, with at least 5 films measured for each sample to obtain the average current-voltage value.

3. Results and discussion

3.1. Characterization of the in-situ growth of TCPP in AAO

FESEM and AFM were employed for the characterization of both the AAO and MOF surfaces to confirm the *in-situ* growth of TCPP in AAO. As shown in Fig. 1a and b, presenting the top view and side view of the AAO, respectively, the AAO exhibited structural arrayed nanochannels. The pore size of AAO was measured to be 88.62 ± 10.60 nm (Fig. S1). Meanwhile, SEM images display the top view and side view of the MOF, respectively, in Fig. 1c and d. The outer surface of the AAO was densely covered by 2D nanosheets (Fig. 1c), and the channels were filled with the dense 2D nanosheets (Fig. 1d) following the *in-situ* growth of TCPP on AAO. Combining Fig. S4, these results indicate that the Al-TCPP has grown on both the inner and outer surfaces of the AAO pores.

AFM was also utilized to characterize the outer surface of the nanochannels before and after the *in-situ* growth. As shown in Fig. 2a−d, a comparison of the AFM images before and after the *in-situ* TCPP growth revealed a noticeable increasement in surface roughness. This increasement strongly suggests the successful growth of MOF 2D nanosheets in the outer surface of AAO. From Fig. 2c and d, the diameter of the nanochannels with successfully modified MOF nanosheets was analyzed using the method outlined in Fig. S2, yielding an average diameter of approximately 12.1 ± 2.3 nm. These results suggest that the modified MOF nanosheets effectively reduce the channel size of AAO.

3.2. Surface properties of aptamer-modified nanochannels

In this work, the ligand TCPP utilized the metallic aluminum present in AAO to serve as

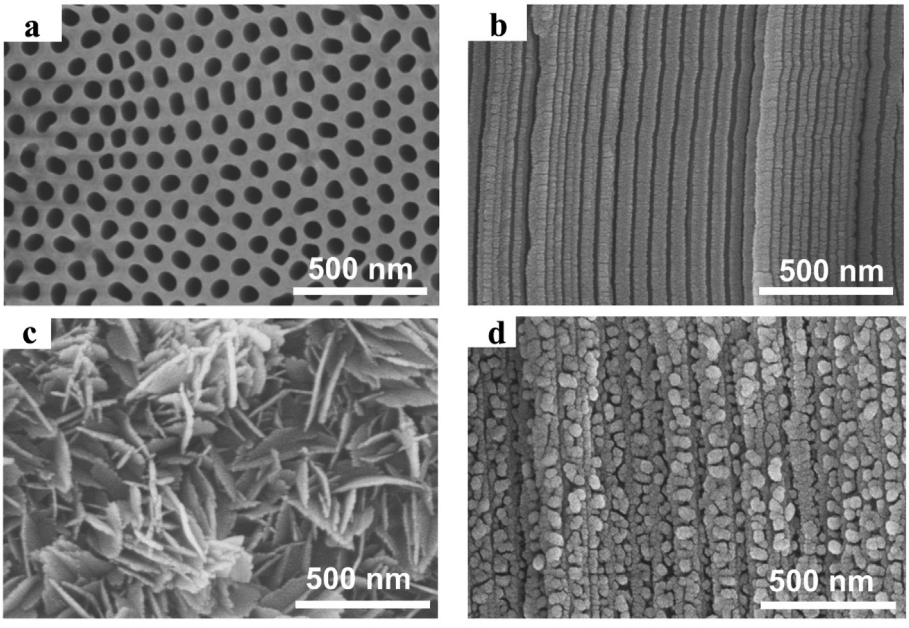

Fig. 1. SEM images of AAO and MOF. (a, b) Top and side views of AAO, respectively. (c, d) Top and side views of MOF, respectively. The images demonstrate the successful in-situ growth of the ligand TCPP on AAO, forming the MOF modified nanochannels and effectively reducing the diameter of the AAO.

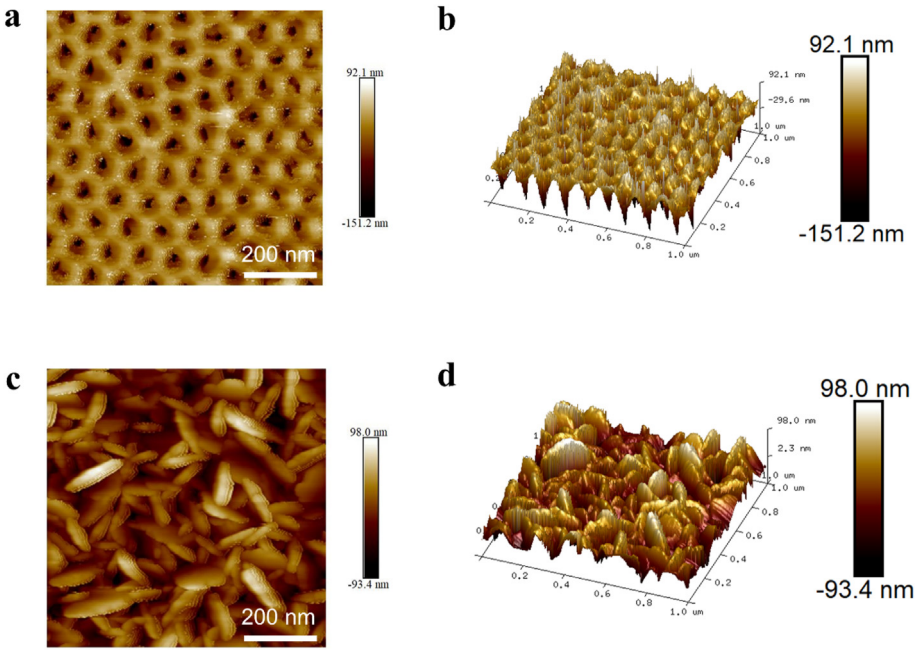

Fig. 2. AFM images and pore size analyses of nanochannels. (a, b) 2D and 3D AFM images of AAO, respectively. (c, d) 2D and 3D AFM images of MOF, respectively. The results further confirm that the MOF nanosheets were successfully grown on the outer surfaces of AAO.

the required metal ions for coupling, enabling the growth of dense MOF 2D nanosheets *in-situ*. Aptamers were employed to modify the AAO and MOF nanochannels by conjugating their amino groups with the carboxyl groups on the nanochannels, which were treated with carboxyl activators. Here, Guanine tetraplexes (G-quadruplexes) were selected as Sr^{2+} specific sensing probes. Guanine tetraplexes are higher-order structures derived from biological sources, formed by folding DNA or ribonucleotides rich in tandem guanine repeats [34]. These structures can be created by stacking two or more G-quadruplexes [35−38]. Studies have shown that in the presence of Sr^{2+}, the linear DNA can be folded into a stable G-quadruplex structure [39,40]. The sensors employed in this study were the resulting APT/AAO and APT/MOF/AAO. To confirm the successful grafting of aptamers onto nanochannels, we carefully analyzed the elemental compositions of AAO, MOF, and APT/MOF/AAO film surfaces using XPS. As shown in Fig. 3a, MOF exhibited N elements compared to AAO, resulting in the presence of an N1s peak. The O1s (532.02 eV) peak exhibited significant enhancement after the successful grafting of aptamers onto the MOF, indicating an increase in the content of O elements (Fig. 3b and c). As shown in Fig. 3d, a distinctive peak of P2p emerged around 133.86 eV, signifying the presence of phosphorus elements from the aptamers on the surface of MOF. Similarly, the N1s (400.98 eV) peak showed a significant enhancement after the aptamer was successfully grafted onto MOF, indicating an increase in the content of N elements (Fig. 3e and f). The heightened intensities of the C−NH_2 and C=O peaks from the bases in the aptamer suggested the successful attachment of aptamers onto the MOF. These XPS findings validate the successful attachment of aptamers onto MOF.

3.3. Sr^{2+} detection performances of ATP/AAO and APT/MOF/AAO

To illustrate the enhanced detection sensitivity of APT/MOF/AAO nanochannels, we tested the *I*−*V* curves with the APT/AAO and APT/MOF/AAO in response to varying concentrations of Sr^{2+}. Upon binding to the target, the initially "stretched" aptamer undergoes a conformational change to form a G-quadruplex structure in response to Sr^{2+} induction. This alteration increases the effective pore size of the nanochannels, and subsequently modifies the ion current passing. As shown in Fig. 4a, the transmembrane ion currents were recorded before and after the immersion in a 100 nmol·L^{-1} Sr^{2+} solution using the APT/MOF/AAO. Following immersion in the ionic solution, the transmembrane current of the APT/MOF/AAO increased from 3.99 μA to 5.80 μA at 1 V, marking an approximate 45% increase in ion current. The increase of current was mainly due to the formation of G-quadruplex induced by Sr^{2+}, triggering a conformational shift in the aptamer within the nanochannels, thereby enlarging the effective channel size and subsequently boosting the

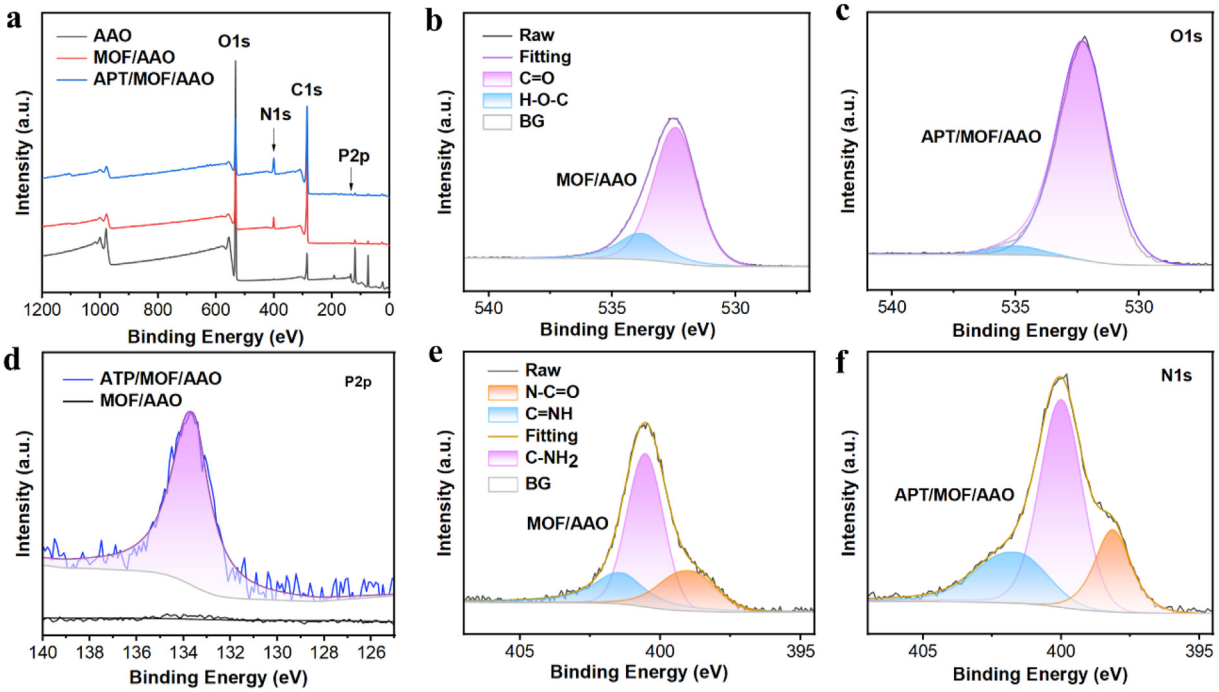

Fig. 3. XPS spectra of AAO, MOF, and ATP/MOF/AAO. (a) Survey spectra of bare AAO, MOF and ATP/MOF/AAO. (b, c) The narrow spectra near the O1s peak for MOF and APT/MOF/AAO. (d) The narrow spectra near the P2p peak for MOF and APT/MOF/AAO. (e, f) The narrow spectra near the N1s peak for MOF and APT/MOF/AAO. The above results show that the aptamers were successfully grafted onto MOF to form APT/MOF/AAO.

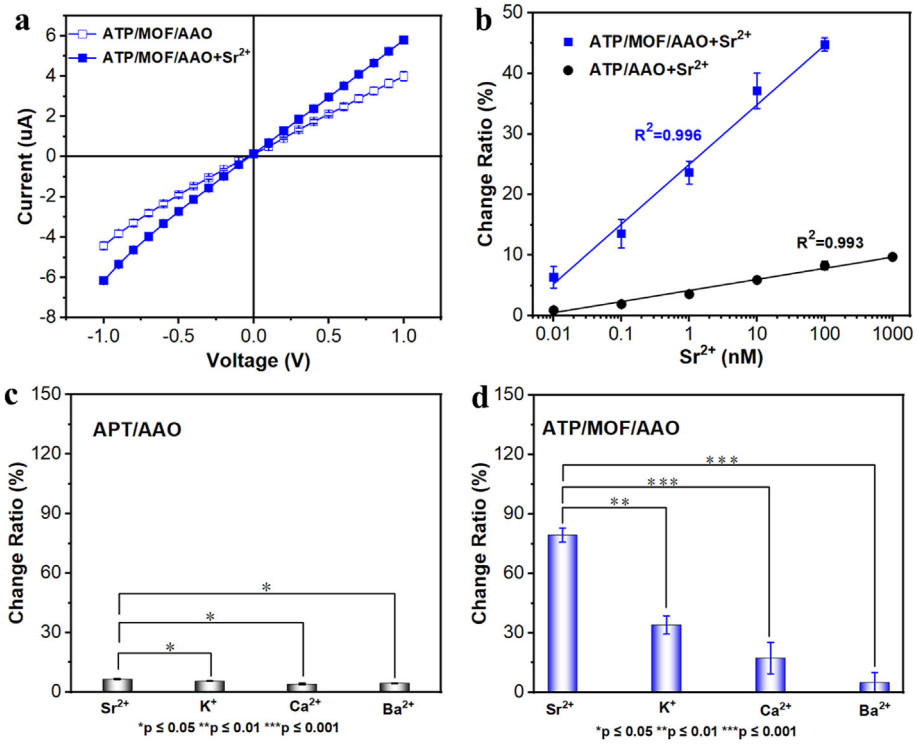

Fig. 4. Sensitivity and specificity of ATP/AAO and ATP/MOF/AAO detections for Sr^{2+}. (a) I—V curves before and after APT/MOF/AAO responses to 100 nmol·L^{-1} Sr^{2+}. After exposure to Sr^{2+}, the APT/MOF/AAO exhibited an increase in ionic current. (b) The relationship plots between the increase in ionic current and the logarithm of Sr^{2+} concentration (0.01, 0.1, 1, 10, 100, and 1000 nmol·L^{-1}) for APT/AAO and APT/MOF/AAO. (c, d) Specificity plots of nanochannels with APT/AAO and APT/MOF/AAO for Sr^{2+} as well as three analogues, including K^{+}, Ca^{2+}, and Ba^{2+}. APT/MOF/AAO demonstrates greatly improve the detection sensitivity and specificity of Sr^{2+}.

current. In the experiment, we defined the transmembrane ion current amplification of the nanochannels as $(I_2-I_1)/I_1 \times 100\%$, where I_1 and I_2 represent the currents before and after detecting the same concentration of the target at 1 V, respectively. In this work, a 10% rise in transmembrane ion current within the nanochannels is deemed a reliable sensing event. Conversely, increases below 10% are considered ineffective, likely due to factors such as physical adsorption or non-specific interactions.

To compare the difference in sensitivity to differential pressure between the APT/AAO and APT/MOF/AAO, the relationship between ion current amplification and Sr^{2+} concentration was analyzed. As shown in Fig. 4b, as the concentration of Sr^{2+} was increased from 0.01 nmol·L^{-1} to 1000 nmol·L^{-1}, the transmembrane ion currents of both the ATP/AAO and ATP/MOF/AAO were increased gradually. For the APT/AAO, the ion current rised from 0.55% to 10%, with increases below 10% deemed invalid. Whereas, in the APT/MOF/AAO, it escalated from 6.37% to 44.74%. Notably, the ion current increase in the APT/MOF/AAO demonstrates a linear correlation with the logarithm of Sr^{2+} concentration. Upon reaching a 10% increase in transmembrane ion current, the Sr^{2+} ion concentrations detected by APT/AAO and APT/MOF/AAO were calculated to be 1000 nmol·L^{-1} and 0.03 nmol·L^{-1}, respectively, indicating the LOD values of APT/AAO and APT/MOF/AAO reached 1000 nmol·L^{-1} and 0.03 nmol·L^{-1}, respectively. Remarkably, the LOD of Sr^{2+} detected by the APT/MOF/AAO was approximately 3.3×10^4 times higher than that of APT/AAO.

To verify the specificity of nanochannels detection for Sr^{2+}, three other solutions containing similar metal ions, namely, K^+, Ca^{2+}, and Ba^{2+}, were chosen. Both the APT/AAO and APT/MOF/AAO were immersed in 100 nmol·L^{-1} solutions of each metal ion, and the resulting ion current increases were recorded. As shown in Fig. 4c, there was no significant difference in the ion current increase observed for the APT/AAO following immersion in solutions composing of the aforementioned selected ions separately. The significance analysis revealed a p-value ranging between 0.01 and 0.05, indicating only marginal statistical significance.

However, for the APT/MOF/AAO, the ion current increase following immersion in the Sr^{2+} solution was significantly higher compared to those in the other three ions solutions (Fig. 4d). The respective current increases were 79.4%, 34.0%, 17.3%, and 4.9% for Sr^{2+}, K^+, Ca^{2+}, and Ba^{2+}. The difference analysis yielded a p-value of less than or equal to 0.01. These findings highlight the remarkable sensing specificity of the APT/MOF/AAO, which exhibited superior specific recognition ability compared to the APT/AAO.

To evaluate the reliability of the APT/MOF/AAO sensing system in real water samples, we added 0, 1, and 10 nmol·L^{-1} Sr^{2+} separately to mineral water, tap water and seawater, respectively, to assess the recovery rate of Sr^{2+} in these three types of water samples. Subsequently, the resulting increase in ion current was recorded. The recovery rate and coefficient of variation (CV) were 94.00%−118.70% and 2.89%−9.35%, respectively (Table 1). These results indicate that the APT/MOF/AAO system exhibited high recovery rate and low variability in real water samples, highlighting its strong detection capabilities in such environments. We also discussed the impact of the sensor system's performance when it is in a high-salt ion solution (Fig. S3). The result indicates that the APT/MOF/AAO sensor system can maintain stable detection performance in high salt ion solutions. Therefore, this sensing method can be applied in real seawater detection.

3.4. Mechanism of enhanced sensing performance of APT/MOF/AAO

To explore the enhanced sensitivity and specificity of Sr^{2+} detection by the APT/MOF/AAO, a classical ionic conductance model is employed. When a voltage is applied, ions in the electrolytic solution are driven by an electric field to pass through the nanochannels, generating a current signal. This sensing system adheres to the universal ion conductivity model based on cylindrical nanochannels, where the ion current (I) in the nanochannels can be expressed by the following formula [41].

$$I = V([n_+\mu_+ + n_-\mu_-]e)\left(\frac{4h}{\Pi D^2} + \frac{1}{D}\right)^{-1} + \frac{V\mu_{\oplus}\Pi D\sigma}{h} \quad (1)$$

Table 1. Recovery of Sr^{2+} in real water samples based on APT/MOF/AAO.

Samples	Added (nmol·L^{-1})	Tested (nmol·L^{-1})	Recovery (%)	CV (%)
Mineral water	0	0.09	–	–
	1	1.03	94.00	4.42
	10	11.96	118.70	9.35
Tap water	0	0.05	–	–
	1	1.00	95.44	5.62
	10	10.63	105.88	4.43
Seawater	0	0.02	–	
	1	1.00	98.28	7.05
	10	11.41	113.88	2.89

Where V represents the transmembrane voltage, h and D represent the thickness and pore size of the nanochannels, respectively, while D is regarded as an effective diameter; n_+, n_- and μ_+, μ_- represent the densities and electrophoretic mobilities of positive and negative ions, respectively; e is the elementary charge; the term $(V\mu_{\oplus}\Pi D\sigma)/h$ represents the ionic current through the highly surface-charged nanochannels. $\mu_{\oplus}$ here represents the mobility of ions in a solution that is opposite to the charged pore charge, and σ is the surface charge density, which is the opposite sign of the opposite ionic charge. Our previous studies have demonstrated that when all electrolyte solutions in the experiment are concentrated at 0.1 mol·L^{-1} and the nanochannels pore size (D) is much smaller than its thickness, Equation (1) can be simplified to the following equation [23].

$$I = V\left(\frac{4h}{\Pi D^2}\right)^{-1} \tag{2}$$

From Equation (2), it can be seen that effective pore size (D) of the nanochnnels significantly influences the transmembrane ion current in the experiment. Thus, we investigated the relationship between the transmembrane ion current and the effective pore size for the APT/AAO or APT/MOF/AAO during detection (Fig. 5).

Before binding to the target, the aptamer within the nanochannels remains in a stretched configuration, causing a hindrance in the nanochannel current. However, owing to the strong binding affinity between Sr^{2+} and G-quadruplex, the aptamer transitions from its stretched state to a more stable G-quadruplex conformation upon Sr^{2+} induction. Consequently, the effective diameter of the nanochannels shifts from d to $d+\Delta d$ (Fig. 5a). Here, we make the assumption that the effective pore size increment before and after binding to the target in both AAO and MOF is the same, denoted as Δd. Upon binding to the target, the effective pore size of the APT/AAO increases from d_1 to $d_1+\Delta d$, while that of the APT/MOF/AAO nanochannels increases from d_2 to $d_2+\Delta d$ (Fig. 5b and c). In the experiment, the increases in ion currents for the APT/AAO and APT/MOF/AAO can be represented as ΔI and $\Delta I'$, respectively, as follows:

$$\Delta I = \frac{I_2 - I_1}{I_1} \tag{3}$$

$$\Delta I' = \frac{I'_2 - I'_1}{I'_1} \tag{4}$$

Where the I_1 and I_2 represent the ion currents before and after the APT/AAO binds to the target, and I'_2 and I'_1 represent the ion currents before and after the APT/MOF/AAO binds to the target. To compare the increase in ion currents between the APT/AAO and APT/MOF/AAO after binding to the target, we calculated the difference between $\Delta I'$ and ΔI as follows:

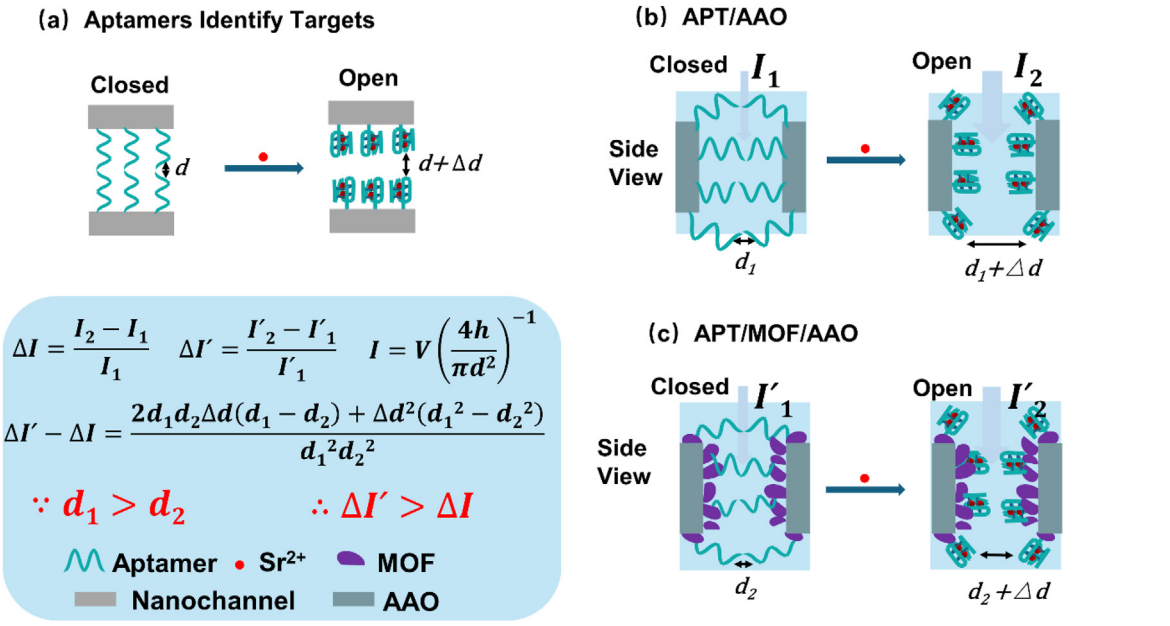

Fig. 5. Schematic diagrams showing the sensing mechanisms of APT/AAO and APT/MOF/AAO. (a) Process of aptamer-modified nanochannel recognition of Sr^{2+}. Before the target is recognized, the aptamer is stretched to clog the nanochannels (Closed), after binding to the target, the aptamer is induced by Sr^{2+}, and the aptamer folds into a G-quadruplex structure to open the nanochannel (Open). As a result, the nanopore diameter changes from d to d+Δd. (b, c) Side views of the APT/AAO and APT/MOF/AAO detection processes, respectively. The results indicate that the APT/MOF/AAO has higher sensitivity than the APT/AAO due to the synergistic effect of 2D nanosheets and specific probes.

$$\Delta I' - \Delta I = \frac{2d_1 d_2 \Delta d(d_1 - d_2) + \Delta d_2 (d_1^2 - d_2^2)}{d_1^2 d_2^2} \quad (5)$$

Through previous SEM and AFM images of APT/MOF/AAO, it was confirmed that the nanochannels were filled and covered with dense layers of 2D nanosheets on the inner walls and outer surfaces of AAO. This feature causes the effective pore size of the APT/MOF/AAO to be much narrower, resulting in a smaller effective pore size than that of the APT/AAO (d_2<d_1). Based on this observation and Eq. (5), when $\Delta I'$-$\Delta I > 0$ is calculated, it becomes evident that the ion current increase of the APT/MOF/AAO surpasses that of the APT/AAO upon binding with Sr^{2+}. These findings suggest that the enhanced sensitivity and specificity of Sr^{2+} detection with the APT/MOF/AAO can be attributed to the reduction of the effective mass transfer pathway within the nanochannels by the 2D nanosheets, along with the synergistic effect of aptamers with the stable structure formed by the target.

3.5. Experimental simulations using COMSOL

To further corroborate our findings, we conducted simulations using COMSOL Multiphysics 6.0. COMSOL modeling diagram of the potential distribution of nanochannels is illustrated in Fig. 6a. This model comprises two cells identical to the top and bottom, with nanochannels situated in the middle. For more detailed parameters of the model, please refer to Fig. S5 and Table S1. The potential within the nanochannels channel gradually diminishes from top to bottom. The nanochannels have diameters of 75, 60, 26, and 10 nm, respectively, with an initial electrolyte concentration of 10 mol·m^{-3}. Given the focus on the synergistic effect from decreased nanochannel's effective diameter by MOF and specific binding of Sr^{2+} by aptamer, the influence of nanochannel surface charge is disregarded in this context. Based on the constructed COMSOL model, the outcomes are displayed in Fig. 6b and c. After Sr^{2+} is recognized by the APT/AAO and APT/MOF/AAO, the ion current is larger than that before recognition. Furthermore, the ionic current change ration before and after the recognition of Sr^{2+} by APT/MOF/AAO nanochannels exceeds that of APT/AAO (Fig. 6d). The ion current change ratio of APT/MOF/AAO was calculated to be 452%, approximately 8.3 times higher than the APT/AAO's 54.5%. This indicates that APT/MOF/AAO is more sensitive than APT/AAO in detecting Sr^{2+}. In conclusion, the calculation results align closely with the experimental results.

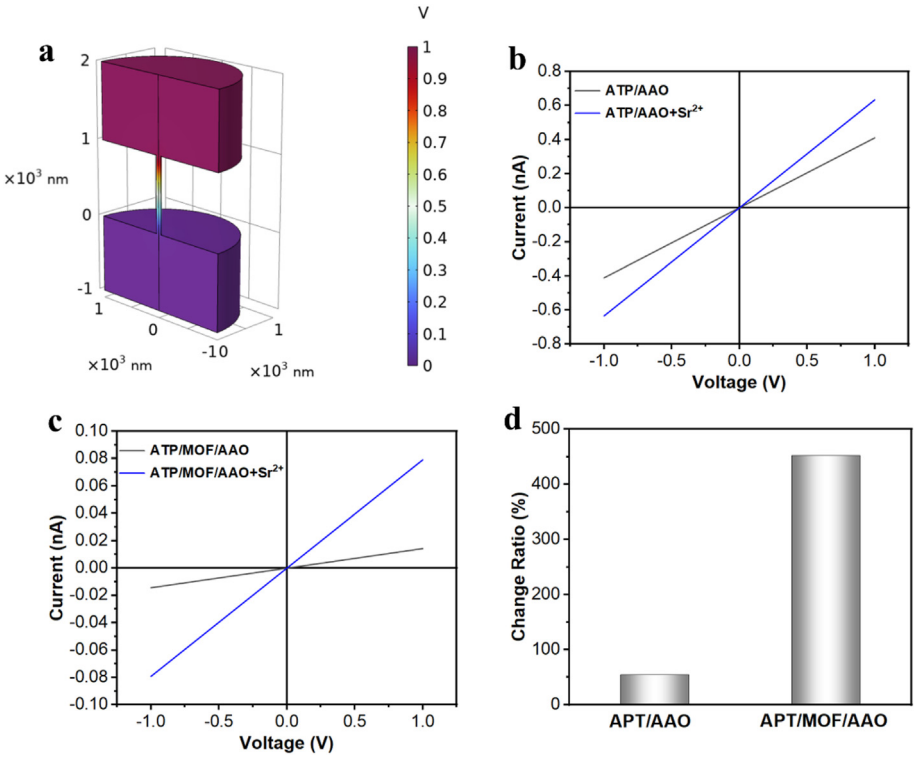

Fig. 6. Simulation results of ionic currents in APT/AAO and APT/MOF/AAO. (a) COMSOL modeling diagram of the potential distribution within nanochannels during testing. (b, c) I—V curves before and after binding to the target for APT/AAO and APT/MOF/AAO, respectively. The current increases after APT/AAO and APT/MOF/AAO bind to the targets. (d) Amplification of ion current ratio graphs after the target recognition by APT/AAO and APT/MOF/AAO. The increase in ion current after recognition of the target by APT/MOF/AAO is much larger than that by APT/AAO.

4. Conclusions

Due to the numerous advantages of the biochemical sensing system in nanochannels, such as fast speed, high sensitivity and specificity, label-free operation, and excellent throughput, the solid-state nanochannels modified with 2D nanomaterials and specific aptamers were designed for the high-sensitivity detection of Sr^{2+}. In the process of Sr^{2+} recognition, the synergistic effect is induced from decreased nanochannel's effective diameter by MOF and specific binding of Sr^{2+} by aptamer, thereby, significantly amplifying the difference in ionic current signals. As a result, the LOD of the APT/MOF/AAO has been reduced from 1000 $nmol \cdot L^{-1}$ to 0.03 $nmol \cdot L^{-1}$ compared to that of the APT/AAO. Furthermore, the sensing mechanism of nanochannels was elucidated using the general ion conductivity model of cylindrical nanochannels, while COMSOL simulations corroborated the increase in ion currents in the nanochannels before and after binding to the target, aligning closely with experimental findings. Additionally, the APT/MOF/AAO also demonstrated robust capability in reliably detecting nanomolar levels of Sr^{2+} in complex samples. This research enhances understanding of the synergistic effects of nanochannels and offers significant insights into developing solid-state nanochannels with higher sensitivity for analyzing samples from complex environments.

Supporting information

Additional information as noted in the text. This material is available free of charge via the internet at https://jelectrochem.xmu.edu.cn/journal/.

Conflict of interest

The authors declare no competing interest.

Acknowledgements

This work was financially supported by the National Natural Science Foundation of China (No. 22090050, No. 22090052, No. 22176180), National Basic Research Program of China (No. 2021YFA1200400), the Natural Science Foundation of Hubei Province (No. 2024AFA001), Shenzhen Science and Technology Program (No. JCYJ20220530162406014).

References

[1] Kaidarova A, Geraldi N R, Wilson R P, Kosel J, Meekan M G, Eguíluz V M, Hussain M M, Shamim A, Liao H, Srivastava M. Wearable sensors for monitoring marine environments and their inhabitants[J]. Nat. Biotechnol., 2023, 41(9): 1208−1220.

[2] da Costa B M, Duarte A C, Rocha-Santos T A P. Environmental monitoring approaches for the detection of organic contaminants in marine environments: A critical review[J]. Trends Environ. Anal. Chem., 2022, 33: e00154.

[3] Alam I, Rehman J U, Ahmad N, Nazir A, Hameed A, Hussain A. An overview on the concentration of radioactive elements and physiochemical analysis of soil and water in Iraq[J]. Rev. Environ. Health, 2020, 35(2): 147−155.

[4] Bolobajev J, Leier M, Vaasma T, Nilb N, Salupere S. Laboratory and pilot plant scale study on the removal of radium, manganese and iron from drinking water using hydrous manganese oxide slurry[J]. J. Environ. Chem. Eng., 2022, 10(6): 108942.

[5] Farouk M IH Z, Jamil Z, Latip M FA. Towards online surface water quality monitoring technology: A review[J]. Environ. Res., 2023, 238(Part1): 117147.

[6] Agberien A V, Örmeci B. Monitoring of cyanobacteria in water using spectrophotometry and first derivative of absorbance[J]. Water, 2019, 12(1): 124.

[7] Xu Z H, Zhou W C, Dong Q C, Li Y, Cai D Y, Lei Y, Bagtzoglou A, Li B K. Flat flexible thin milli-electrode array for real-time *in situ* water quality monitoring in distribution systems[J]. Environ. Sci.-Wat. Res. Technol., 2017, 3(5): 865−874.

[8] Uppuluri K, Szwagierczak D, Fernandes L, Zaraska K, Lange I, Synkiewicz-Musialska B, Manjakkal L. A high-performance pH-sensitive electrode integrated with a multi-sensing probe for online water quality monitoring[J]. J. Mater. Chem. C, 2023, 11(44): 15512−15520.

[9] Lu Y K, Li P F, Yan H Y, Shen S G. Ionic liquid modified porous polymer as a dispersive filter extraction adsorbent for simple, sensitive, and efficient determination of chlorotriazine herbicides in irrigation water[J]. J. Agric. Food Chem., 2022, 70(4): 1327−1334.

[10] Izquierdo J EE, Cavallari M R, García D C, Oliveira J DD S, Nogueira V AM, Braga G DS, Ando Junior O H, Quivy A A, Kymissis I, Fonseca F J. Detection of water contaminants by organic transistors as gas sensors in a bottom-gate/bottom-contact cross-linked structure[J]. Sensors, 2023, 23(18): 7981.

[11] Novaes C G, Bezerra M A, da Silva E GP, dos Santos A MP, da Silva Romao I L, Neto J HS. A review of multivariate designs applied to the optimization of methods based on inductively coupled plasma optical emission spectrometry (ICP OES)[J]. Microchem. J., 2016, 128: 331−346.

[12] Li Q, Ying Y L, Liu S C, Lin Y, Long Y T. Detection of single proteins with a general nanopore sensor[J]. ACS Sens., 2019, 4(5): 1185−1189.

[13] Ying Y L, Gao R, Hu Y X, Long Y T. Electrochemical confinement effects for innovating new nanopore sensing mechanisms[J]. Small Methods, 2018, 2(6): 1700390.

[14] Long Y T, Zhang M N. Self-assembling bacterial pores as components of nanobiosensors for the detection of single peptide molecules[J]. Sci. China, Ser. B: Chem., 2009, 52(6): 731−733.

[15] Yang H, Qing G. Solid-state nanopores and nanochannels for the detection of biomolecules[J]. Chem. Phys. Rev., 2021, 2(2): 021306.

[16] Shen F Y, Dow W P, Liu A H, Lin J Y, Chang P H, Huang S M. Periodic pulse reverse Cu plating for through-hole filling[J]. ECS Electrochem. Lett., 2013, 2(5): D23−D25.

[17] Hou X, Zhang H C, Jiang L. Building bio-inspired artificial functional nanochannels: From symmetric to asymmetric modification[J]. Angew. Chem. Int. Ed., 2012, 51(22): 5296−5307.

[18] Deng J Q, Liu C, Sun J S. DNA-based nanomaterials for analysis of extracellular vesicles[J]. Adv. Mater. 2023: 2303092.

[19] Bodily T A, Ramanathan A, Wei S, Karkisaval A, Bhatt N, Jerez C, Haque M A, Ramil A, Heda P, Wang Y. In pursuit of degenerative brain disease diagnosis: dementia biomarkers detected by DNA aptamer-attached portable graphene biosensor[J]. Proc. Natl. Acad. Sci. U.S.A., 2023, 120(47): e2311565120.

[20] Ban D K, Liu Y, Wang Z, Ramachandran S, Sarkar N, Shi Z, Liu W, Karkisaval A G, Martinez-Loran E, Zhang F. Direct DNA methylation profiling with an electric biosensor[J]. ACS Nano, 2020, 14(6): 6743−6751.

[21] Wang J, Hou J, Zhang H C, Tian Y, Jiang L. Single nanochannel-aptamer-based biosensor for ultrasensitive and selective cocaine detection[J]. ACS Appl. Mater. Interfaces, 2018, 10(2): 2033−2039.

[22] Ma Q, Chu W J, Nong X L, Zhao J, Liu H, Du Q J, Sun J L, Shen J L, Lu S M, Lin M H, Huang Y, Xia F. Local Electric potential-driven nanofluidic ion transport for ultrasensitive biochemical sensing[J]. ACS Nano, 2024, 18(8): 6570−6578.

[23] Liu L X, Luo C H, Zhang J H, He X, Shen Y, Yan B, Huang Y, Xia F, Jiang L. Synergistic effect of bio-inspired nanochannels: Hydrophilic DNA probes at inner wall and hydrophobic coating at outer surface for highly sensitive detection[J]. Small, 2022, 18(37): 2201925.

[24] Meng D, Hao C L, Cai J R, Ma W, Chen C, Xu C L, Xu L G, Kuang H. Tailored chiral copper selenide nanochannels for ultrasensitive enantioselective recognition and detection[J]. Angew. Chem. Int. Ed., 2021, 133(47): 25201−25208.

[25] Zeng H, Zhou S, Xie L, Liang Q R, Zhang X, Yan M, Huang Y A, Liu T Y, Chen P, Zhang L, Liang K, Jiang L, Kong B. Super-assembled mesoporous thin films with asymmetric nanofluidic channels for sensitive and reversible electrical sensing[J]. Biosens. Bioelectron., 2023, 222: 114985.

[26] Qiao Y J, Hu J J, Hu Y X, Duan C, Jiang W L, Ma Q, Hong Y N, Huang W H, Xia F, Lou X D. Detection of unfolded cellular proteins using nanochannel arrays with probe-functionalized outer surfaces[J]. Angew. Chem. Int. Ed., 2023, 62(43): 202309671.

[27] Han B, Chakraborty A. Highly efficient adsorption desalination employing protonated-amino-functionalized MOFs [J]. Desalination, 2022, 541: 116045.

[28] Cheng P, Liu Y L, Wang X P, Fan K M, Li P, Xia S J. Regulating interfacial polymerization via constructed 2D metal-organic framework interlayers for fabricating nanofiltration membranes with enhanced performance[J]. Desalination, 2022, 544: 116134.

[29] Ying Y P, Zhang Z Q, Peh S B, Karmakar A, Cheng Y D, Zhang J, Xi L F, Boothroyd C, Lam Y M, Zhong C L, Zhao D. Pressure-responsive two-dimensional metal-organic framework composite membranes for CO_2 separation[J]. Angew. Chem. Int. Ed., 2021, 60(20): 11318−11325.

[30] Doustkhah E, Hassandoost R, Khataee A, Luque R, Assadi M HN. Hard-templated metal-organic frameworks for advanced applications[J]. Chem. Soc. Rev., 2021, 50(5): 2927−2953.

[31] Qiu M, Zhu Z P, Wang D Y, Xu Z, Miao W N, Jiang L, Tian Y. Large-scale metal-organic framework nanoparticle monolayers with controlled orientation for selective transport of rare-earth elements[J]. J. Am. Chem. Soc., 2023, 145(22): 12275−12283.

[32] Ingram B, Sloan D. Strontium isotopic composition of estuarine sediments as paleosalinity-paleoclimate indicator [J]. Science, 1992, 255(5040): 68−72.

[33] Jiang Y, Ma W J, Qiao Y J, Xue Y F, Lu J H, Gao J, Liu N N, Wu F, Yu P, Jiang L, Mao L Q. Metal-organic framework membrane nanopores as biomimetic photoresponsive ion channels and photodriven ion pumps[J]. Angew. Chem. Int. Ed., 2020, 59(31): 12795−12799.

[34] Huang H, Suslov N B, Li N S, Shelke S A, Evans M E, Koldobskaya Y, Rice P A, Piccirilli J A. A G-quadruplex−containing RNA activates fluorescence in a GFP-like fluorophore[J]. Nat. Chem. Biol., 2014, 10(8): 686−691.

[35] Pu F, Wu L, Ran X, Ren J S, Qu X G. G-quartet-based nanostructure for mimicking light-harvesting antenna[J]. Angew. Chem. Int. Ed., 2015, 54(3): 892−896.

[36] Biffi G, Tannahill D, McCafferty J, Balasubramanian S. Quantitative visualization of DNA G-quadruplex structures in human cells[J]. Nat. Chem., 2013, 5(3): 182−186.

[37] Lin Y T, Wang M L, Hsu C F, Dow W P, Lin S M, Yang J J. Through-hole filling in a Cu plating bath with functional insoluble anodes and acetic acid as a supporting electrolyte [J]. J. Electrochem. Soc., 2013, 160(12): D3149−D3153.

[38] Trajkovski M, Webba da Silva M, Plavec J. Unique structural features of interconverting monomeric and dimeric G-quadruplexes adopted by a sequence from the intron of the N-myc gene[J]. J. Am. Chem. Soc., 2012, 134(9): 4132−4141.

[39] Akhshi P, Mosey N J, Wu G. Free-energy landscapes of ion movement through a g-quadruplex DNA channel[J]. Angew. Chem. Int. Ed., 2012, 12(124): 2904−2908.

[40] Kankia B I, Marky L A. Folding of the thrombin aptamer into a G-quadruplex with Sr^{2+}: stability, heat, and hydration[J]. J. Am. Chem. Soc., 2001, 123(44): 10799−10804.

[41] Wanunu M. Nanopores: A journey towards DNA sequencing[J]. Phys. Life Rev., 2012, 9(2): 125−158.

金属有机框架功能化的纳米通道对锶离子进行高灵敏度检测

王旭刚[a]，何正旭[a]，丁德芳[a]，罗雪芹[a]，戴　力[a]，张炜奇[a]，马　群[b]，黄　羽[a,*]，夏　帆[a,c]
[a]中国地质大学材料科学与化学学院，纳米地质材料教育部工程研究中心，生物地质与环境地质国家重点实验室，湖北 武汉 430074
[b]大阪都立大学研究生院工学研究科化学工程系，日本 大阪堺市 599-8570
[c]中国地质大学深圳研究院，广东 深圳 518052

摘要

锶-90 是一种高放射性同位素，在食物链和骨骼结构中积累，对人类健康构成重大风险。在复杂的环境水样中，迫切需要一种高灵敏的锶-90 检测策略。在这里，金属有机框架（metal organic frameworks）和特异性适配体修饰的固态纳米通道被设计用于高灵敏度的 Sr^{2+}检测。MOF 导致的纳米通道有效孔径减小与适配体对 Sr^{2+}的特异性结合之间的协同作用放大了离子电流信号的差异，显著提高了检测灵敏度。MOF 修饰的纳米通道对 Sr^{2+}表现出高灵敏度的检测，检测限（LOD）低至 0.03 $nmol·L^{-1}$，没有修饰 MOF 纳米片的 AAO 的 LOD 仅为 1000 $nmol·L^{-1}$。结果表明，MOF 修饰的纳米通道对 Sr^{2+}的检测限 LOD 比未修饰 MOF 的纳米通道高约 33,000 倍，仿真模拟计算结果与这一实验趋势完全吻合。此外，加标回收实验实现了对各种水样中 Sr^{2+}的高度可靠性检测，回收率在 94.00%至 118.70%之间，变异系数低至 2.89%至 9.35%之间。APT/MOF/AAO 传感系统在真实水样中表现出高回收率和低变异性，凸显了其在此类环境中的强大检测能力。这项研究为快速发展的先进纳米通道传感器领域及其在分析复杂样品方面包括环境污染物检测、食品分析、医疗诊断等的各种应用提供了宝贵的见解。

关键字：纳米通道；金属有机框架；传感器；锶离子；高灵敏检测